Communication

Single Photon Approach for Chirality Sensing

Fabrizio Sgobba [1] **, Arianna Elefante** [1] **, Stefano Dello Russo** [1] **, Mario Siciliani de Cumis** [1,2]
and Luigi Santamaria Amato [1,3,*]

[1] Italian Space Agency (ASI), Centro Spaziale 'Giuseppe Colombo', Località Terlecchia, 75100 Matera, Italy;
    fabrizio.sgobba@asi.it (F.S.); arianna.elefante@asi.it (A.E.); stefano.dellorusso@asi.it (S.D.R.)
[2] Istituto Nazionale di Ottica, Consiglio Nazionale delle Ricerche, L.go E. Fermi 6, 50125 Firenze, Italy
[3] Istituto Nazionale di Ottica, CNR-INO, Via Campi Flegrei n. 34 Pozzuoli (NA), 80078 Pozzuoli, Italy
*   Correspondence: luigi.santamaria@asi.it

Abstract: We developed a high sensitivity optical sensor for circular birefringence using a heralded photon source. The sensor can be employed for chirality measurements and, being based on single photons, can be exploited for fragile biological sample or in metrological applications where the light intensity must be kept as low as possible. We found the best operational condition; then, we calibrated the sensor and tested its performance up to a very long acquisition time, obtaining excellent stability and a sub-ppm birefringence detection limit (for a 100 μm sample), thus paving the way for fundamental physics test as well.

Keywords: circular birefringence; single photon; chirality; polarization measurement

1. Introduction

Chirality in nature can be found at any scale, from the world of subatomic particles all the way up to the cosmological scales.

An object is referred to as chiral if its structure is non-superimposable with its own mirror image. The natural occurrence of chirality can be associated with the laws of parity-invariance [1], whose violation, demonstrated experimentally by Wu et al. [2] in 1957, represented a milestone for the development of modern physics of elementary particles and their interactions.

At the molecular scale, chirality manifests itself with the formation of enantiomers, molecules with the same chemical structure but opposite chirality. Parity invariance suggests that molecular energy levels have to be identical for both enantiomers. However, an energy discrepancy between the two ground states in the order of magnitude of 0.1–1 feV is expected to occur due to parity violation.

The experimental observation of the predicted energy discrepancy between enantiomers ground states still represents one of the greatest challenges to contemporary stereochemistry [3,4].

Chirality also plays an important role in the field of biochemistry and pharmacology because of the paradigm of 'homochirality' [5], i.e., the exclusive preference of one specific enantiomeric form of certain molecules to constitute the building blocks of all forms of life. Moreover, since its detection could be a strong evidence for the existence of extraterrestrial life, homochirality has a vital role in astrobiology [6,7].

Far from being confined to academia and fundamental research, the study and detection of chirality has an important role in widely applicative fields such as pharmacology or food and the beverage industry [8].

Approximately 56% of the pharmaceuticals currently produced and commercialized involve chiral molecules, and 88% of those are administered through racemic proportions [9]. Despite having the same chemical structure, in racemic drugs, the enantiomers usually show different biological effects (such as toxicity) [10,11]; therefore, the American

Food and Drug Administration (FDA) requires new compounds to be produced as single enantiomers, whereas non-abiding cases are usually addressed one by one [12,13]. Moreover, chirality detection and sensing is involved in biomedical applications, being helpful in the diagnosis of kidney diseases [14], infectious diseases [15] or mental disorders [16].

Chiral structures' interaction with light is polarisation-dependent (a phenomenon known as optical activity). High-sensitivity optical techniques are therefore well-suited to be among the best performing chirality sensing techniques [17,18].

A first way optical activity may present itself is through dichroism [19], i.e, a polarisation dependency of the imaginary part of the refractive index, resulting in a polarisation-dependent absorption.

If the optical activity affects the real part of the refractive index (the propagation velocity of light through the medium), the phenomenon is called birefringence [19] instead.

Optical rotatory dispersion (ORD) is an optical technique that senses chiral objects employing birefringence [20]. When a linearly polarized light (LPL), that can be seen as composed of equal amount of left (LCP) and right circular polarized (RCP) light, impinges on the sample, the LCP and RCP components are de-phased since these propagate at different velocities inside the sample (circular birefringence). The induced RCP-LCP dephasing can therefore be measured outside the sample as a rotation in the linear polarization of a certain angle θ, which results in:

$$\theta = \frac{\pi l}{\lambda}[n_{LC} - n_{RC}] \tag{1}$$

where l is the length of the sample, λ the test laser beam wavelength and $n_{LC} - n_{RC}$ the optical circular birefringence (n_{LC}, n_{RC} is the refractive index for Left, Right polarized light) [21,22].

Since such birefringence is usually as weak as one part on 10^6, the most common way to improve the detection limit relies either on employing high-power lasers to enhance the signal-to-noise ratio (SNR) or on increasing the optical path length inside the sample, for example, by means of optical cavities [22]. Another approach consists in employing balanced heterodyne detection to average out common noise [21].

Unfortunately, for biological samples, where the high source intensities may trigger undesired reactions [23], the laser power must be kept as low as possible to avoid degradation, especially for long acquisition times. The same holds true in meteorological applications [24], where the source must be kept as low-power as possible to avoid system perturbation. These application needs inspired the development of quantum meteorological techniques for birefringence detection in the recent past.

These quantum approaches, which aim to improve the precision while keeping the probe beam in the regime of low intensity (down to single-photon levels) [25], enable promising performances [26,27] and, in principle, the possibility to overcome the standard quantum limit [28,29]. Moreover, the employment of a twin correlated photon source greatly reduces the dark counts, which are not negligible, especially in the long wavelength range [27,30].

In quantum polarimetry, as in its high intensity counterpart, the sample chirality is detected by measuring the transmittance of a linearly polarised light passing through the analyte resolved in its polarised components. The presence of the chiral medium rotates the quantum state polarisation and induces a change in the trasmitted intensity, de facto mapping a polarisation rotation into a trasmission intensity measurement. Since the defined Fock states $|N>$ carry no uncertainty in intensity, these states are the best possible choice for transmission intensity measurement [31].

In this paper, we develop a sensor to measure the polarisation rotation induced by a birefringent sample using correlated single photon states in telecom range produced via spontaneous parametric down conversion (SPDC).

Our work extends the results recently obtained at shorter wavelenght to the telecom range [32,33], paving the way for quantum-metrological birefringence measurement in fully

fibre-cabled setups, according to similar developments in the field of Hong-Ou-Mandel interferometry [34,35].

2. Materials and Methods

Experimental Setup

The proposed sensor employs a twin photon source (TPS, 1. with respect to Figure 1) equipped with an internal continuous wave (CW) laser pump with center emission wavelength at 775 nm illuminating a periodically poled litium-niobate (PPLN) crystal optimized to achieve the best performances for type-II spontaneous parametric down conversion (SPDC) at 1550 nm when stabilised in temperature at 33.9 °C.
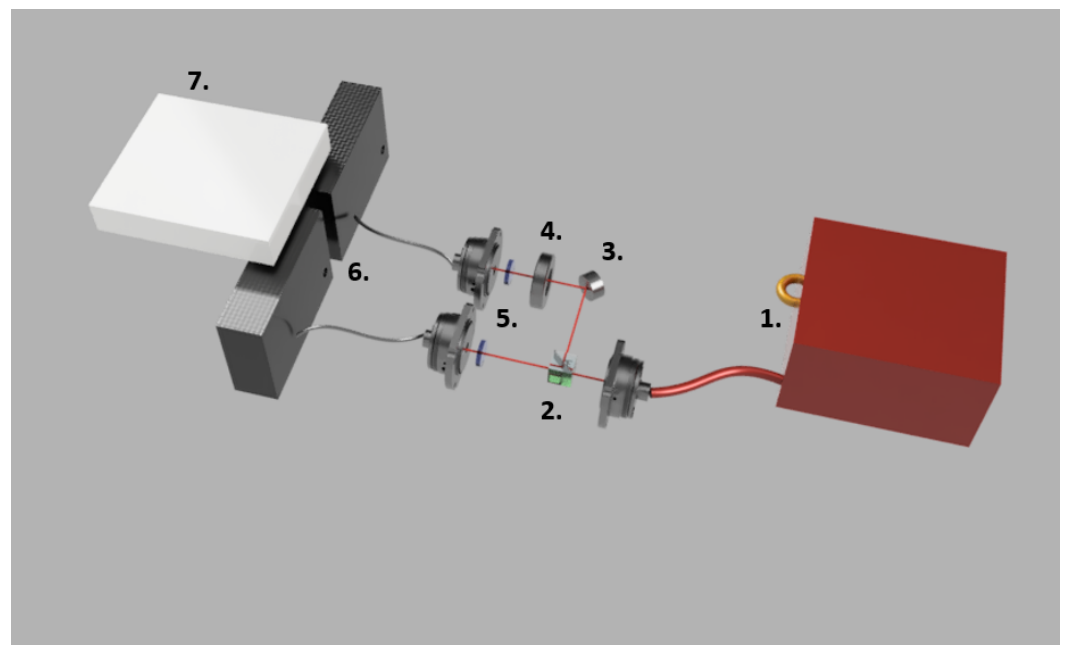
Figure 1. Pictorial 3D representation of the polarisation rotation sensor. (**1.**) Twin photon source, (**2.**) balanced beam splitter, (**3.**) gold-coated plane mirror, (**4.**) half-wave plate (HWP) mounted on motorized rotational stage, acting as polarisation tilting sample, (**5.**) linear polarisers, (**6.**) single photon avalanche diodes detectors (SPADs). (**7.**) Time tagger for coincidence detection. This figure was obtained via Fusion 360.

Each twin photon pair impinges on a balanced beam splitter (BS); therefore, each photon undergoes one of the two output paths with equal probability. Two near-infrared absorbing linear polarisers (extinction ratio of 10^{-5}) are then used to post-select the desired measurement base on the block sphere right before each beam is coupled back into fibres by means of collimating fibre-coupling ports.

The sample is represented by a half-wave plate (HWP, 4. in Figure 1) able to emulate the polarization rotation of a chiral medium with great accuracy and repeatability (the employed HWP introduces retardance of 0.5λ with an error of $\pm 0.01\lambda$ within the signal-idler emission bandwidth). The plate is mounted on a rotational stage and placed on one of the two arms, which will be hereafter referred to as "test arm".

Coupled beams are sent to termo-electrically cooled single photon avalanche diode (SPAD) detectors (6. in Figure 1) connected to a time-tagging device to record single counts on each detector and coincidence counts between detectors (7. in Figure 1). Both SPADs detectors were kept at a 20% detection efficiency and 5 μs dead time, which resulted in $DK_1 \approx 3300$ dark counts per 2 s on channel 1 and $DK_2 \approx 5300$ dark counts per 2 s on channel 2. It is worth noting, however, that the meaningful measurements involve the coincidence counting. Dark counts on coincidence events, given mostly by spurious electric signals triggering one channel within the same coincidence window of a true event on the

other channel, are found to be negligible. The overall resolution of the system composed of the two detectors and the time tagger is ≈100 ps, which is why a coincidence window of 200 ps has been chosen for the experiment.

The introduction of a balanced beam splitter to separate incoming photon pairs into a test beam and a reference beam, instead of a polarising beam splitter, halves the total amount of obtainable coincidences. On the other hand, it ensures that both arms are identical and enables the sampling of all polarization directions in both arms. It avoids systematic errors that may occur for samples (cuvette, optics) with different responses for the vertical and horizontal axes, whereas pure circular birefringence has identical responses for the vertical and horizontal axes.

3. Results and Discussion

3.1. Characterisation of Twin Photon Pairs Mixture

In order to infer the best operative range for the proposed sensor, a first characterisation without a sample has been carried out. The coincidence counts $C(\theta_1, \theta_2)$ have been mapped as a function of the angle the transmission axis of each polariser forms with the horizontal plane (θ_1 and θ_2 for test and reference arm respectively). Since each polariser has been mounted on a motorised rotational stage, the processes of angle assignment, data acquisition and extraction have been automated using LabVieW software. The nested for-loops were designed to operate identical $N_s = 91$ steps of $\delta\theta = 2°$, for an acquisition time of 2 s per single step. The whole measurement lasted ≈4.5 h.

The resulting map is shown in Figure 2.
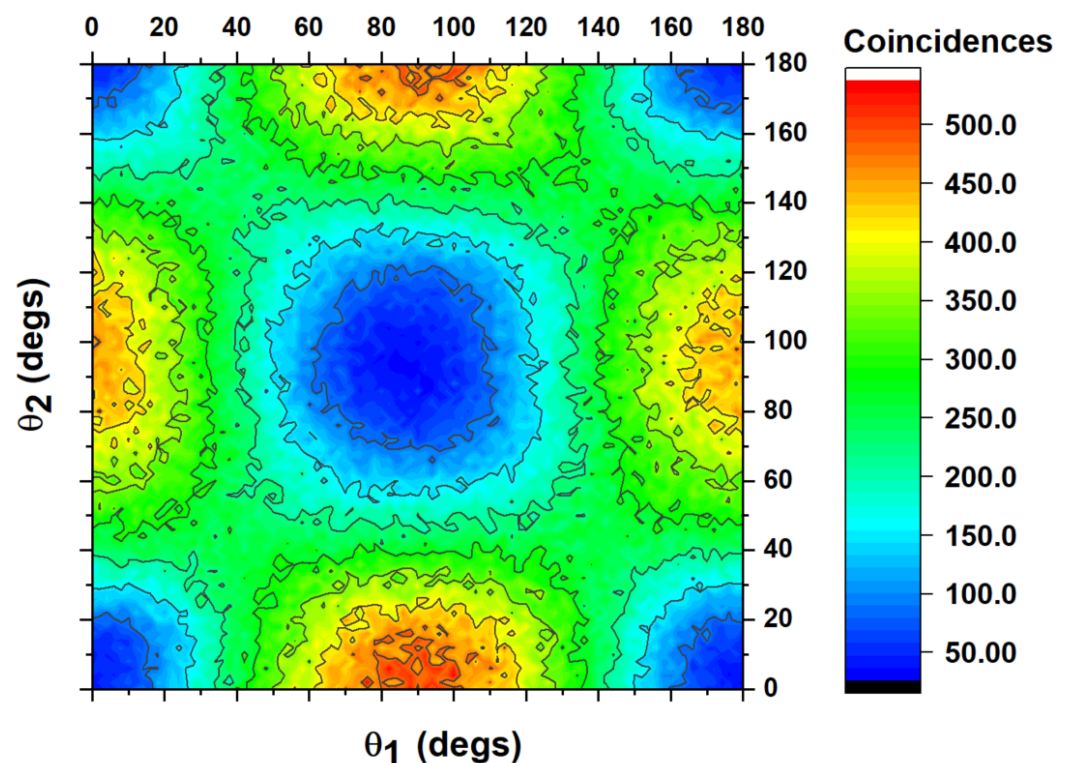
Figure 2. Contour map employed to infer sensor's best operative range. Coincidence counts are mapped as function of polarisation angle of each polariser with respect to horizontal axes, namely θ_1, θ_2.

From Figure 2, it can be observed that $\theta_1 = 90°$ represents the 1D projection with the highest peak-to-throat excursion in $C(\theta_2)$. Thus, in the following, it has been kept fixed: $\theta_1 = 90°$.
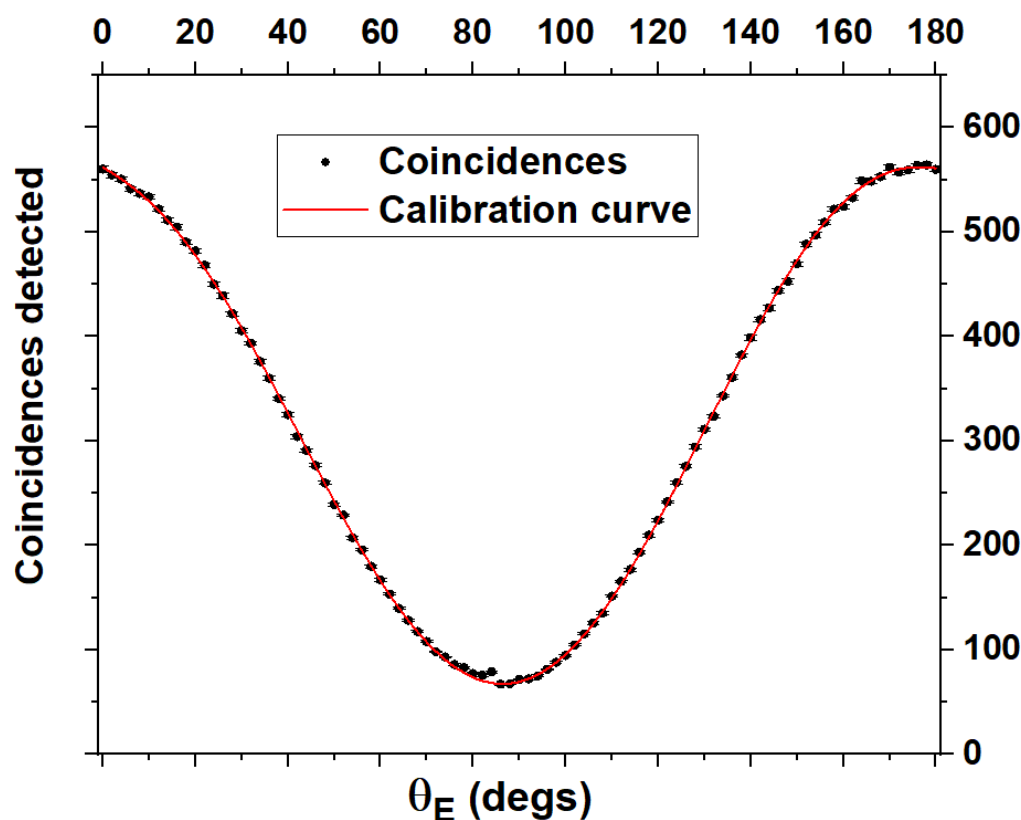
3.2. Calibration of Polarisation Sensor

The proper calibration of the polarisation sensor has been performed, keeping the polariser on the reference arm fixed at $\theta_1 = 90°$, and the polariser placed in the target arm fixed at $\theta_2 = 0°$. A motorised half-wave plate (HWP) has been placed in the target arm, acting as a birefringence sample (4. in Figure 1). To avoid confusion, θ_E will be identified from now as the angle that the electric field forms with the horizontal axis once a horizontally polarised photon has passed the HWP. Such an angle is twice the angle that the HWP forms with the same axis.

Similarly to the previous step, the process of rotation and acquisition has been automated, acquiring $N_s = 91$ steps of $\delta\theta_E = 2°$, for an acquisition time of 2 s per single step, repeating the process for $N_r = 100$ consecutive loops. This measurement session lasted ≈ 5 h.

The coincidence counts in correspondence with each HWP angle have been averaged over the 100 loops, and plotted in Figure 3 with their uncertainty (standard deviation over square root of loops number). To calibrate the sensor, the following polynomial function has been employed:

$$C(\theta_E) = C_0 + \sum_{k=1\ldots6} C_k \left(\frac{\pi(\theta_E - \theta_{E0})}{180} \right)^k$$

Figure 3. Averaged value of $C(\theta_E)$ (black dots) and its uncertainty. The polynomial function employed for calibration is also resported (red curve).

The calibration curve allows one to retrieve the induced rotation of the polarisation as an estimation parameter $\theta_E(C)$, a function of the coincidences measured. The contributions to the offset C_0 are mostly given by fibers and HWP-induced elliptical distortions.

The statistical error committed in the estimation of the chosen parameter at the acquisition time $\tau_a = 2$ s can be inferred using the following equation:

$$\sigma_\theta(\tau_a) \simeq \left\| \frac{\partial \theta_E}{\partial C} \delta C(\tau_a) \right\| \simeq \left\| \frac{\partial \theta_E}{\partial C} \sigma_C(\tau_a) \right\| \tag{2}$$

$\sigma_C(\tau_a)$ has been evaluated as the standard deviation of the measured coincidences at a fixed θ_E. Since $C(\theta_E)$ is not injective in the whole 180° range, being symmetrical with respect to its center $\theta_{E0} = 86°$, the function has been inverted (numerically) piecewise for $\theta_E < \theta_{E0}$ and $\theta_E \geq \theta_{E0}$.

The statistical error $\sigma_\theta(\tau_a)$ on the estimated parameter, evaluated using Equation (2), is presented in Figure 4 as a function of the actual angles reproduced with the rotational mount (θ_E).
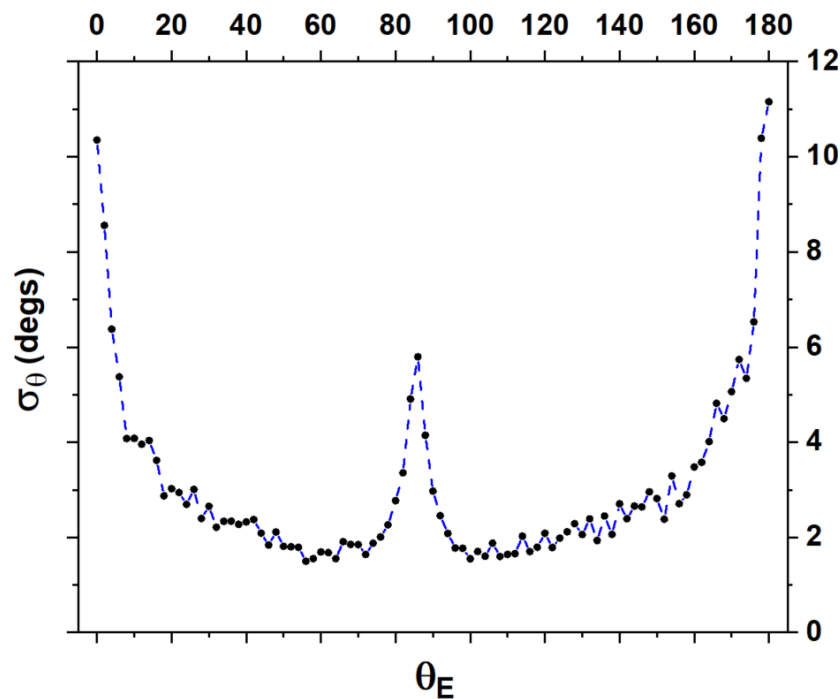
Figure 4. Plot of the statistical error on the estimation parameter $\sigma_\theta(2s)$ (black dots) as a function of the actual angles reproduced with the rotational mount (θ_E).
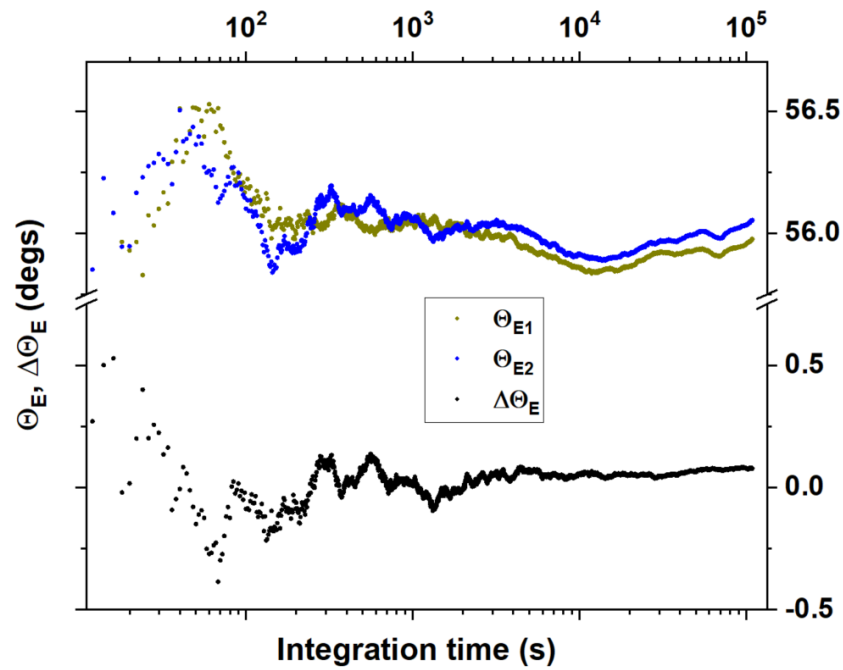
3.3. Minimum Detection Limit

As can be observed in Figure 4, one of the minima for σ_θ falls at $\theta_{E1} \simeq 56°$, where $\sigma_\theta(2s) < 2°$. This value is therefore ideal to perform a long-term measurement. The system has been kept running, acquiring coincidence counts and tilting the motorised HWP between $\theta_{E1} = 56°$ and $\theta_{E2} = 56.1°$, for >60 h over the weekend, acquiring 108,600 datapoints, 54,300 for each angle at $\tau = 2$ s acquisition time. The $\Delta\theta$ has been chosen as the minimum rotation possible outside the sensibility error of the motorised rotational stage itself.

The acquired coincidence counts $C(\theta_{E1}, t_i)$ and $C(\theta_{E2}, t_i + \tau)$ have been converted to the estimation parameter via the inverted function $\theta_E(C)$. The integral average of the estimation parameter $\theta_{E1/2}$ can be defined as follows:

$$\Theta_{E1/2}(T) = \frac{1}{T} \sum_{t=0...T} \theta_{E1/2}(C(t))$$

In addition, it is reported in Figure 5.

As can be observed from Figure 5, the sensor is capable of detecting the variation in polarisation angle after 2 h (i.e., after 2 h, Θ_{E1} and Θ_{E2} no longer intersect with each other).

Figure 5. Integral average of $\Theta_{E1}(T)$ (blue dots), $\Theta_{E2}(T)$ (dark yellow dots), and their difference $\Delta\Theta_E(T)$ (black dots) as a function of integration time, expressed in logarithmic scale.

3.4. Allan Deviation Analysis and Minimum Detection Limit

The most rigorous way to determine the sensor stability at different integration times is to perform a non-overlapping Allan deviation analysis that allows one to infer how the standard deviation of a signal varies at different integration times starting from a single long-term acquisition.

The non-overlapping Allan deviation analysis has therefore been performed over the 53,400 samples of $\Delta\theta_E$ collected over the 60-h-long acquisition. Since this sensor has been devised and designed to measure the optical activity (OA) of circularly birefringent samples, the standard deviation has been converted to optical activity detection limit (OADL), defined as the OA giving unitary signal to noise ratio. From Equation (1), it follows:

$$OADL = \frac{\lambda \sigma_{\theta_E}}{l\pi}$$

In Figure 6, the OADL per unit length (black straight curve), is reported as a function of the average coincidence events acquired, roughly 216 per τ_0, where $\tau_0 = 2$ s. Average coincidence events are a better indicator than integration time since these do not rely on detectors performances. Better detection systems, for example superconducting nanowires single photon detectors (SNSPDs), usually have far lower dead time and higher accuracy levels with respect to SPADs, allowing one to achieve comparable OADL at significantly inferior integration times. The Allan deviation analysis of Θ_{E1}, Θ_{E2} is also reported in Figure 6, here multiplied by a factor $\frac{\lambda}{\pi}$ for comparison (blue and dark yellow straight curves). As can be observed, for sufficiently high numbers of coincidence events acquired, the Allan deviations of Θ_{E1} and Θ_{E2} show a long-term rise significantly deviating from the theoretical limit baseline ($\frac{\sigma}{\sqrt{N_c}}$). This rise is associated in the literature (see for example [36]) with long-term fluctuations of the optical pump. The comparative measurement, $\sigma_{\Delta\Theta}$ (black straight curve), proves to be capable of averaging out this noise contribution.
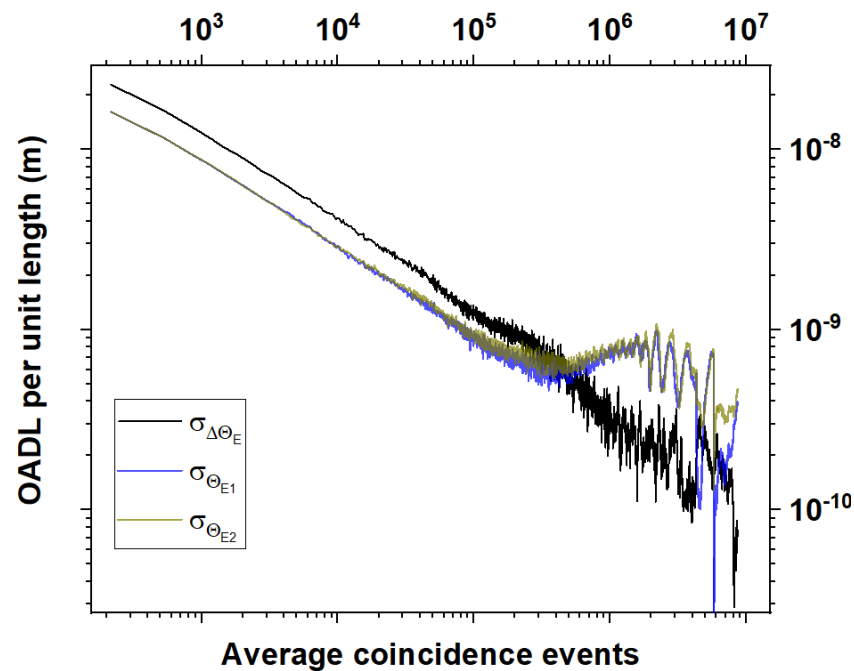
Figure 6. OADL per unit length as a function of the average coincidence events (black curve). The Allan deviation of the single Θ_E is also reported for comparison, respecting the same legend as in Figure 5.

To offer a straightforward comparison with the existing literature, in [21], using high-power sources, an $OADL \approx 8.5 \times 10^{-10}$ has been reached employing an optical path length of $l = 100$ μm. Our sensor shows detection limit three orders of magnitude larger employing a sample with the same path length. It is noteworthy, however, how these results are obtained in the single-photon regime, which makes the proposed sensor extremely attractive especially when used in combination with more efficient and fast detectors (e.g., SPSDC) that are capable to reduce integration times by up to two orders of magnitude.

4. Conclusions

In this paper, we have proposed a highly stable, high-performing sensor based on a twin photon source capable to detect a linear polarisation rotation as low as in the range of hundreds of μrad, taking advantage of the high stability offered by the coincidence counting together with the dual arm configuration.

Having been designed and implemented to operate in the telecom range, the devised sensor represents a significantly innovative step towards fibre-cabled portable twin-photon source-based meteorology devices meant to offer ultra-high precision measurements of chemical or biological samples in a laboratory-controlled environment. Moreover, the sensor has shown to be capable of reaching an accuracy in the measurement of Δn within three orders of magnitude with respect to the one obtained in the literature employing high power sources, in an optical range less suitable to photonics integration.

References

1. Barron, L.D. From Cosmic Chirality to Protein Structure: Lord Kelvin's Legacy. *Chirality* **2012**, *24*, 879–893. [CrossRef]
2. Wu, C.S.; Ambler, E.; Hayward, R.W.; Hoppes, D.D.; Hudson, R.P. Experimental Test of Parity Conservation in Beta Decay. *Phys. Rev.* **1957**, *105*, 1413–1415. [CrossRef]
3. Quack, M.; Seyfang, G.; Wichmann, G. Perspectives on parity violation in chiral molecules: Theory, spectroscopic experiment and biomolecular homochirality. *Chem. Sci.* **2022**, *13*, 10598–10643. [CrossRef]
4. Quack, M. How Important is Parity Violation for Molecular and Biomolecular Chirality? *Angew. Chem. Int. Ed.* **2002**, *41*, 4618–4630. [CrossRef] [PubMed]
5. Walker, S.I. Homochirality. In *Encyclopedia of Astrobiology*; Springer: Berlin/Heidelberg, Germany, 2014; pp. 1–3. [CrossRef]
6. Glavin, D.P.; Burton, A.S.; Elsila, J.E.; Aponte, J.C.; Dworkin, J.P. The Search for Chiral Asymmetry as a Potential Biosignature in our Solar System. *Chem. Rev.* **2019**, *120*, 4660–4689. [CrossRef]
7. Avnir, D. Critical review of chirality indicators of extraterrestrial life. *New Astron. Rev.* **2021**, *92*, 101596. [CrossRef]
8. Nunez, M.; Garcia-Rubino, M.; Conejo-Garcia, A.; Cruz-Lopez, O.; Kimatrai, M.; Gallo, M.; Espinosa, A.; Campos, J. Homochiral Drugs: A Demanding Tendency of the Pharmaceutical Industry. *Curr. Med. Chem.* **2009**, *16*, 2064–2074. [CrossRef] [PubMed]
9. Ceramella, J.; Iacopetta, D.; Franchini, A.; Luca, M.D.; Saturnino, C.; Andreu, I.; Sinicropi, M.S.; Catalano, A. A Look at the Importance of Chirality in Drug Activity: Some Significative Examples. *Appl. Sci.* **2022**, *12*, 10909. [CrossRef]
10. Drayer, D.E. Pharmacodynamic and pharmacokinetic differences between drug enantiomers in humans: An overview. *Clin. Pharmacol. Ther.* **1986**, *40*, 125–133. [CrossRef]
11. Patočka, J.; Dvořák, A. Biomedical aspects of chiral molecules. *J. Appl. Biomed.* **2004**, *2*, 95–100. [CrossRef]
12. Calcaterra, A.; D'Acquarica, I. The market of chiral drugs: Chiral switches versus de novo enantiomerically pure compounds. *J. Pharm. Biomed. Anal.* **2018**, *147*, 323–340. [CrossRef] [PubMed]
13. Daniels, J.M.; Nestmann, E.R.; Kerr, A. Development of Stereoisomers (Chiral) Drugs: A Brief Review Of Scientific and Regulatory Considerations. *Drug Inf. J.* **1997**, *31*, 639–646. [CrossRef]
14. Kimura, T.; Hamase, K.; Miyoshi, Y.; Yamamoto, R.; Yasuda, K.; Mita, M.; Rakugi, H.; Hayashi, T.; Isaka, Y. Chiral amino acid metabolomics for novel biomarker screening in the prognosis of chronic kidney disease. *Sci. Rep.* **2016**, *6*, 26137. [CrossRef]
15. Batalla, P.; Martín, A.; López, M.Á.; González, M.C.; Escarpa, A. Enzyme-Based Microfluidic Chip Coupled to Graphene Electrodes for the Detection of D-Amino Acid Enantiomer-Biomarkers. *Anal. Chem.* **2015**, *87*, 5074–5078. [CrossRef] [PubMed]
16. MacKay, M.A.B.; Kravtsenyuk, M.; Thomas, R.; Mitchell, N.D.; Dursun, S.M.; Baker, G.B. D-Serine: Potential Therapeutic Agent and/or Biomarker in Schizophrenia and Depression? *Front. Psychiatry* **2019**, *10*, 11–17. [CrossRef] [PubMed]
17. Chen, Y.H.; Yang, J.T. A new approach to the calculation of secondary structures of globular proteins by optical rotatory dispersion and circular dichroism. *Biochem. Biophys. Res. Commun.* **1971**, *44*, 1285–1291. [CrossRef]
18. Gogoi, A.; Konwer, S.; Zhuo, G.Y. Polarimetric Measurements of Surface Chirality Based on Linear and Nonlinear Light Scattering. *Front. Chem.* **2021**, *8*, 21–25. [CrossRef]
19. Nakanishi, K.; Berova, N; Woody, R.W. Circular Dichroism: Principles and Applications. VCH Publishers, Inc., New York, NY. 1994. xvii + 576 pp. 15.5 × 23.5 cm. $125.00. ISBN 1-56081-618-X. *J. Nat. Prod.* **1996**, *59*, 1219. [CrossRef]
20. Eyring, H.; Liu, H.C.; Caldwell, D. Optical rotatory dispersion and circular dichroism. *Chem. Rev.* **1968**, *68*, 525–540. [CrossRef]
21. Chou, C.; Tsai, H.M.; Liao, K.Y.; Chou, L.D.; Huang, P.H. Optical activity measurement by use of a balanced detector optical heterodyne interferometer. *Appl. Opt.* **2006**, *45*, 3733. [CrossRef]
22. Vollmer, F.; Fischer, P. Ring-resonator-based frequency-domain optical activity measurements of a chiral liquid. *Opt. Lett.* **2006**, *31*, 453. [CrossRef] [PubMed]
23. Neuman, K.C.; Chadd, E.H.; Liou, G.F.; Bergman, K.; Block, S.M. Characterization of Photodamage to Escherichia coli in Optical Traps. *Biophys. J.* **1999**, *77*, 2856–2863. [CrossRef] [PubMed]
24. Taylor, M.A.; Bowen, W.P. Quantum metrology and its application in biology. *Phys. Rep.* **2016**, *615*, 1–59. [CrossRef]
25. Roccia, E.; Cimini, V.; Sbroscia, M.; Gianani, I.; Ruggiero, L.; Mancino, L.; Genoni, M.G.; Ricci, M.A.; Barbieri, M. Multiparameter approach to quantum phase estimation with limited visibility. *Optica* **2018**, *5*, 1171. [CrossRef]
26. Giovannetti, V.; Lloyd, S.; Maccone, L. Advances in quantum metrology. *Nat. Photonics* **2011**, *5*, 222–229. [CrossRef]
27. Russo, S.D.; Elefante, A.; Dequal, D.; Pallotti, D.K.; Amato, L.S.; Sgobba, F.; de Cumis, M.S. Advances in Mid-Infrared Single-Photon Detection. *Photonics* **2022**, *9*, 470. [CrossRef]
28. Giovannetti, V.; Lloyd, S.; Maccone, L. Quantum-Enhanced Measurements: Beating the Standard Quantum Limit. *Science* **2004**, *306*, 1330–1336. [CrossRef]

29. Wolfgramm, F.; Vitelli, C.; Beduini, F.A.; Godbout, N.; Mitchell, M.W. Entanglement-enhanced probing of a delicate material system. *Nat. Photonics* **2012**, *7*, 28–32. [CrossRef]
30. Elefante, A.; Russo, S.D.; Sgobba, F.; Amato, L.S.; Pallotti, D.K.; Dequal, D.; de Cumis, M.S. Recent Progress in Short and Mid-Infrared Single-Photon Generation: A Review. *Optics* **2023**, *4*, 13–38. [CrossRef]
31. Adesso, G.; Dell'Anno, F.; Siena, S.D.; Illuminati, F.; Souza, L.A.M. Optimal estimation of losses at the ultimate quantum limit with non-Gaussian states. *Phys. Rev. A* **2009**, *79*, 040305. [CrossRef]
32. Tischler, N.; Krenn, M.; Fickler, R.; Vidal, X.; Zeilinger, A.; Molina-Terriza, G. Quantum optical rotatory dispersion. *Sci. Adv.* **2016**, *2*. [CrossRef]
33. Yoon, S.J.; Lee, J.S.; Rockstuhl, C.; Lee, C.; Lee, K.G. Experimental quantum polarimetry using heralded single photons. *Metrologia* **2020**, *57*, 045008. [CrossRef]
34. Harnchaiwat, N.; Zhu, F.; Westerberg, N.; Gauger, E.; Leach, J. Tracking the polarisation state of light via Hong-Ou-Mandel interferometry. *Opt. Express* **2020**, *28*, 2210. [CrossRef] [PubMed]
35. Sgobba, F.; Pallotti, D.K.; Elefante, A.; Russo, S.D.; Dequal, D.; de Cumis, M.S.; Amato, L.S. Optimal Measurement of Telecom Wavelength Single Photon Polarisation via Hong-Ou-Mandel Interferometry. *Photonics* **2023**, *10*, 72. [CrossRef]
36. Giglio, M.; Patimisco, P.; Sampaolo, A.; Scamarcio, G.; Tittel, F.K.; Spagnolo, V. Allan deviation plot as a tool for quartz-enhanced photoacoustic sensors noise analysis. *IEEE Trans. Ultrason. Ferroelectr. Freq. Control* **2015**, *63*, 555–560. [CrossRef]